MIT Libraries | DSpace@MIT

MIT Open Access Articles

*A novel bearingless interior permanent magnet slice motor for pump**

The MIT Faculty has made this article openly available. ***Please share*** how this access benefits you. Your story matters.

Citation: Kant, Krishan, Weinreb, Benjamin S., Hegy, Michael, Gartner, Mark and Trumper, David L. 2022. "A novel bearingless interior permanent magnet slice motor for pump*." IFAC-PapersOnLine, 55 (27).

As Published: 10.1016/j.ifacol.2022.10.533

Publisher: Elsevier BV

Persistent URL: https://hdl.handle.net/1721.1/154889

Version: Final published version: final published article, as it appeared in a journal, conference proceedings, or other formally published context

Terms of use: Creative Commons Attribution-NonCommercial-NoDerivs License

Massachusetts Institute of Technology

Available online at www.sciencedirect.com
ScienceDirect
IFAC PapersOnLine 55-27 (2022) 323–328

A novel bearingless interior permanent magnet slice motor for pump ⋆

Krishan Kant * **Benjamin S. Weinreb** ** **Michael Hegy** **
Mark Gartner ** **David L. Trumper** *

* *Massachusetts Institute of Technology, Cambridge, MA 02139 USA (e-mail: kkbhalla@mit.edu).*
** *Ension Inc., Butler, PA 16002 USA*

Abstract: A 2 pole bearingless interior permanent magnet (IPM) motor with slice rotor configuration is presented in this paper. A novel IPM rotor is designed considering various specifications such as force constant, torque constant and cogging torque. Cogging torque and resulting vibrations affects the motor and levitation operation significantly. Since the cogging torque is a result of the motor geometry, finite element (FE) simulation is used to simulate various rotor geometries to find the desired rotor configuration. FE simulations are also used to obtain other parameters like force and torque constant, and magnetic stiffness for designing control. The final design is fabricated and tested for closed loop levitation control and speed control. The simulation results and experimental control system performance is shown and explained in the paper.

Copyright © 2022 The Authors. This is an open access article under the CC BY-NC-ND license (https://creativecommons.org/licenses/by-nc-nd/4.0/)

Keywords: Bearingless motor, buried magnets, pump, finite element simulation.

1. INTRODUCTION

Bearingless motor operates as a motor with the rotor levitated. This motor doesn't require any components like bearing, seals, shaft etc. The rotor can operate in a sealed housing and this makes this motor very attractive for pump applications with low contamination.

Bearingless motor topologies are presented in the literature for pump application as well other applications (1; 2; 3). These include motors like surface mount, interior permanent magnet motors, flux switching motors, reluctance motors, hysteresis motors and induction motors. Among these, permanent magnet bearingless motors are more popular because of relatively compact size and better efficiency owing to better levitation and torque capability. As a specific stator flux interaction with the rotor flux produces torque, similarly a different stator flux can be generated to produce a force in rotor plane (4). This can be achieved by either adding another set of the windings in the stator, or injecting separate coils with different currents to generate required torque and force (5).

For pump application, a slice rotor configuration is preferred. A slice rotor is characterised by a small axial length to diameter ratio of the rotor. During levitation, this gives the advantage of positive passive axial and tilt stiffness produced by the attractive force between the stator steel and permanent magnets in rotor, thereby providing stability in those degrees of freedom without active control (1; 6).

In this paper, a 2 pole IPM rotor topology is used. IPM rotor has buried magnets which provides better mechanical robustness whereas surface mount permanent magnet rotors requires a retaining mechanism for the magnets. There is literature available which explores the IPM bearingless motors since these provides easier way to approach the tradeoff between force and torque generation (3). But since this motor has inherent asymmetry in magnetic structure, it produces different force at different rotor alignments as well as varying negative stiffness in different orientations. In (7; 8), authors have tried to minimize these differences via rotor designs. But such rotor design has relatively large cogging torque owing to the magnetic structure, which leads to operational issues such as position fluctuation at higher speeds. Some other reasons for position fluctuation are investigated and implemented as discussed in (7; 9). But these methods are not very effective and it led to the conclusion that a new rotor topology has to be designed.

This paper addresses the issue of cogging torque and position fluctuations during operation while maintaining the required pump specifications. The finalized rotor design is fabricated and tested for levitation and motor operation using closed loop position and speed control. The control performance along with the control design is discussed in the paper. The Hall effect sensors are placed in the motor to provides the angular position measurement and a speed estimator is designed with measured angle as input for the speed control. The experimental results of levitation and speed control system performance is shown and discussed in this paper.

2. OPERATION OF BEARINGLESS PM MOTOR

Torque generation in an IPM motor with 2 pole rotor requires a rotating 2 pole stator flux synchronized with the rotor orientation. This is provided by a 2 pole 3 phase

⋆ This work is sponsored by National Institutes of Health (NIH) under Award 5R42HL134455.

2405-8963 Copyright © 2022 The Authors. This is an open access article under the CC BY-NC-ND license.
Peer review under responsibility of International Federation of Automatic Control.
10.1016/j.ifacol.2022.10.533

stator winding. Ideally, this winding should produce zero average force on the rotor. It is established in the literature (4) that to generate a radial force on a p pole rotor, a $p \pm 2$ pole stator flux is required. To generate a force in arbitrary direction in the rotor plane, a similarly rotating/arbitrarily oriented stator flux is required, which can be implemented using three phase, 4 pole winding. For synchronous motors, the torque production can be understood as stator flux locking with rotor flux with same pole number (p). But force generation using $p \pm 2$ pole can be understood as shown in Fig. 1.

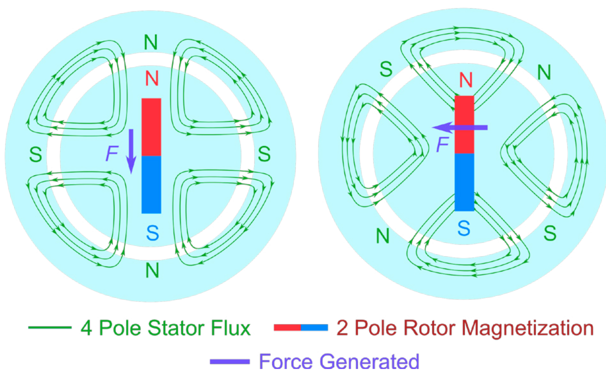

Fig. 1. Force generation in a 2 pole bearingless motor. 4 pole stator flux required to generate force is shown as green flux lines. Figures show how to generate orthogonal force in two axes via stator flux orientation with respect to fixed rotor orientation.

As mentioned earlier, apart from torque and force requirement, the cogging torque requirement for this motor is also important for stable pump operation. Since various requirements are coupled, the following design philosophy is considered for the IPM motor to reduce the coupling between various design parameters. The force constant, torque constant, radial stiffness and cogging torque, all depend on airgap flux; but cogging torque is significantly dependent on geometry as well. Airgap flux density can be modified fairly independently from cogging torque by keeping the same geometry and increasing the magnet thickness. Thicker magnets may result in more reluctance variation around the rotor periphery because of bigger magnet slot, but fundamental geometry will remain the same. Cogging torque can be reduced by modifying the magnetic geometry of the rotor and stator. Since for this paper, the stator is fixed, only the rotor design is modified to improve the performance.

3. ROTOR DESIGN

For this motor design, a previously fabricated stator is used which has 2 pole and 4 pole windings. The stator structure and winding details are briefly discussed later in this paper. More details can be found in (7; 10). As discussed earlier, the primary performance parameter in this section is cogging torque and the rotor is designed using finite element simulation program (ANSYS).

Various 2 pole rotor structures are evaluated for cogging torque using 3D FE simulations. As discussed earlier the cogging torque of the IPM motor depends on the stator saliency and rotor saliency due to magnets and saturated bridges. Since the rotor is 2 pole, all the buried magnets will be chords in the rotor to avoid flux shorting by the rotor steel. The way these chords reach the airgap and their location affect the cogging torque. As a check, the dimensions and shape of bridges are also varied as part of design iterations. Some of these designs along with their associated cogging torque values are shown in Fig.2. As shown in Fig.2, a design with the minimum cogging torque is selected and fabricated for prototype.

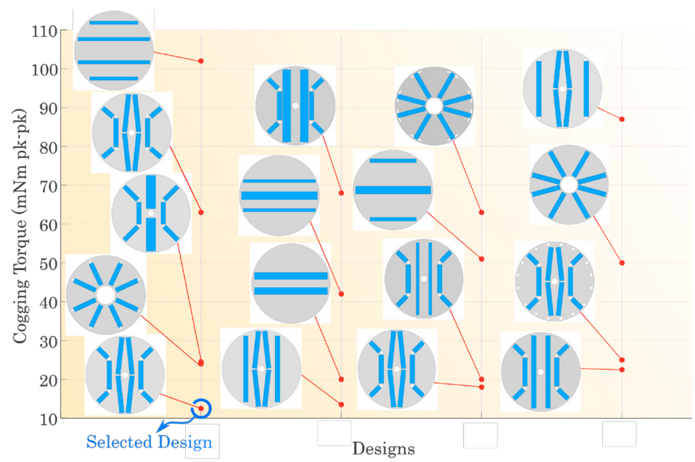

Fig. 2. Various rotor geometry configurations and associated peak to peak cogging torque value. Designs are shown in columns set along horizontal axis. Red dot shown associated cogging torque values. The selected design in highlighted. More details are given in (9) .

4. MOTOR COMPONENTS AND FABRICATION

The basic dimensions of the motor are obtained from previous designs and pump specifications. The active length of the rotor and stator is 10mm, the rotor outer diameter is kept 50 mm while stator inner diameter is 54mm. This makes a 2mm airgap in the motor which is required for fitting the pump housing, impeller body and still have reasonable space for fluid flow. Few details of the arrangement and construction of stator, winding and sensors are discussed here and more details can be found in (7; 10).

4.1 Stator

As mentioned earlier, the stator has a three phase 2 pole winding to produce the torque and a three phase four pole winding to produce in force in orthogonal direction to acheive levitation. To accommodate both these windings, a 12 teeth stator with temple design is used. This stator, as shown in Fig.3, is being reused from a previous motor since it fits the requirements nicely (7). The stator is fabricated as L shaped pieces from steel laminates fitted inside a stator back iron which have slots to accommodate these pieces, thereby making a temple type design. The back iron is a laminated disk made of steel to magnetically connect all the stator teeth.

4.2 Winding

Two pole motor winding and four pole suspension winding are both 3 phase windings and are mounted on 12 stator

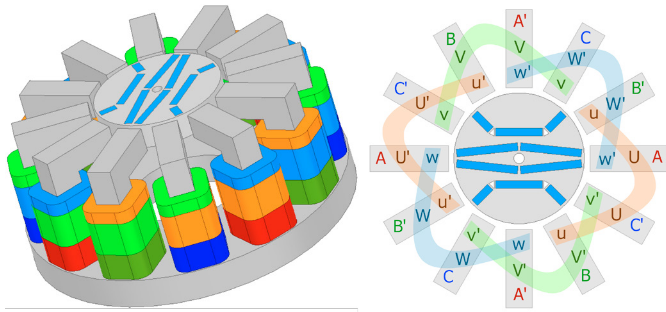

Fig. 3. Motor with temple stator and associated winding connections shown on the right. Each tooth has 3 coils with 2 upper coils for motor operation and a lowest coil for force generation. Upper 2 layers, UVW *and* $uvw - 2$ pole motor winding and Bottom layer, $ABC - 4$ pole levitation winding. $A'B'C'$ refers to reversed winding polarity. All the coils in one phase of either motor or levitation winding are connected in series, the colored connections in the motor winding shows the 2 pole arrangement. The colored belts show series connection with polarity specified by apostrophe('). UVW has 140 turns, uvw has 52 turns and ABC has 108 turns.

teeth. A 4 pole winding will have a 60° mechanical angle between consecutive phases which can be easily wound on a 12 teeth stator. Similarly a 2 pole winding will require 120° between consecutive phases. The windings are concentrated, so each coil will be wound on one teeth, which can cause a large harmonic content in the airgap flux. Thus multiple windings are used in each phase of 2 pole winding to make the flux distribution closer to sinusoidal. The final winding arrangement is shown in Fig.3

4.3 Sensors

The pump operation requires implementing stable levitation as well as rotation torque, which is achieved using a closed loop control system. The controlled degrees of freedom are the radial X, Y positions as well as angular position. The other three rigid body degrees of freedom (Z, θ_X, θ_Y) are passively stabilized via magnetic stiffnesses. In this topology, optical sensors are used to measure the X/Y position of the rotor. The optical sensors are placed between the stator teeth and require a reflective surface to measure the distance to the rotor. A white tape is used around the rotor peripheral surface to establish a diffuse reflective surface for the optical sensor. The X, Y position is measured differentially using 4 optical sensors placed in diametrically opposite positions between the stator teeth. The angular position and thereby speed is measured using Hall effect sensors to sense the rotor magnetic field. These sensors are fitted on printed circuit boards (PCBs) which are placed on the top and bottom of the stator teeth near the air gap. A total of 12 Hall effect sensors are used, 6 on top PCB and 6 on bottom PCB to measure the angular position of the rotor.

4.4 Rotor

The finalized rotor topology (Fig. 2) is fabricated using solid steel rotor by machining the magnet and bridge slots

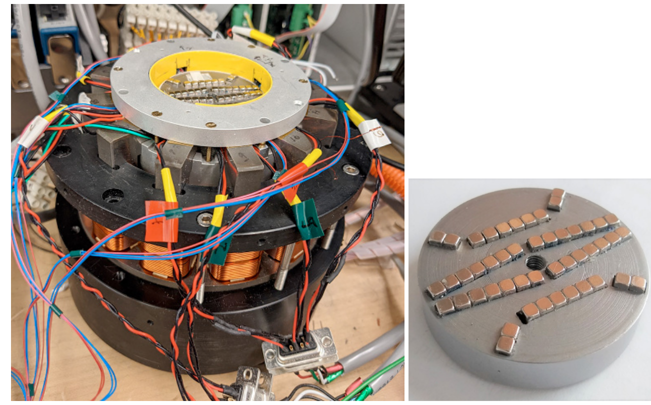

(a) (b)

Fig. 4. (a) Bearingless motor assembly showing the temple stator with windings and the rotor inside the stator bore (b) New rotor design with off the shelf magnets to achieve the designed magnetic geometry.

in this. A solid rotor was used in the prototype to allow easy fabrication of the prototype, although it will have the issue of eddy current generation while operation. But since the magnets are buried in the rotor, the relatively large magnet flux will not vary in the rotor frame while the rotor is rotating and thus does not induce rotor eddy currents. However, the stator flux does vary in the rotor frame when the rotor rotates. Since the stator flux is much smaller than the magnet flux, the rotor experiences a relatively small flux variation and thus the eddy currents in the rotor are not significant. The magnets used in the rotor are $12.7 \times 3.175 \times 3.175\ mm$ (1/2" × 1/8" × 1/8") N48 grade magnets. These are block magnets and rotor slots are adjusted to fit these magnets available off the shelf without affecting the magnetic performance significantly.

The final motor assembly with newly designed rotor is shown in Fig. 4.

5. CONTROL SYSTEM DESIGN AND PERFORMANCE

This section explains the system parameters estimation from finite element (FE) simulation, levitation control architecture, verification of the control system design for desired performance, thereby completing the levitation control of the motor. It further discusses the closed loop motor speed control.

5.1 Parameter estimation from FE simulation

The X,Y position and motor torque of the motor needs to controlled in closed loop. For that, the levitated system must be understood and characterized before designing the controller. The torque and force generating capabilities of the new rotor is verified against minimum specifications during the rotor design iteration. The force and torque capability is obtained for final design using simulation and is shown in Fig. 5. Since the rotor is 2 pole and have an inherent asymmetry in the structure, the force and torque generation capacity at different rotor angular positions is not the same. This causes a force and torque ripple with operation under three phase sinusoidal currents, but this effect becomes insignificant when the rotor is levitated and centered. Thus the force and torque constants can be obtained from Fig. 5. Apart from these, the negative radial stiffness of the rotor in X and Y direction are also obtained from the simulations as mentioned in Table 1. The performance of levitation operation with rotation is shown in Fig. 6 where a constant current command is given with appropriate commutation to generate force in Y direction.

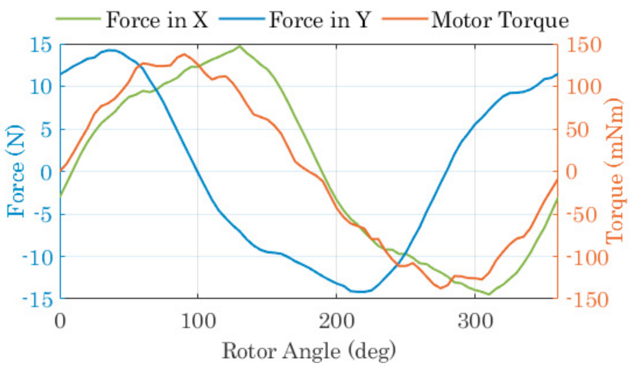

Fig. 5. Simulated force and torque generation with static 3 phase currents in both windings (1 A rms) . The actual currents in all windings will be $I_{U,u,A} = 1.414A$, $I_{V,v,B} = -0.707A$, $I_{W,w,C} = -0.707$.

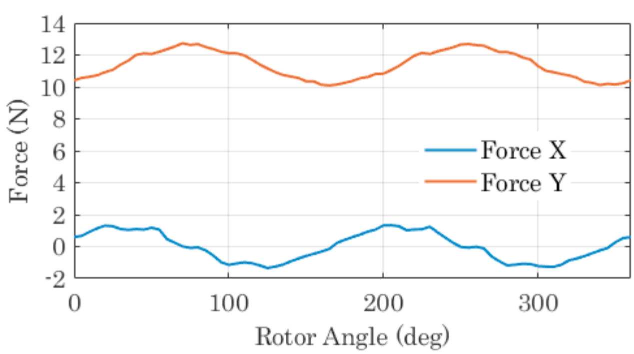

Fig. 6. Simulated force generation for $1A_{rms}$ (i_{ABC}) with current commutation corresponding to commanded force generation in Y. Parasitic coupling to X position is apparent. Although the average force in X direction is zero over one rotor rotation, there is parasitic force which is present in both X and Y forces due to the reasons described earlier.

5.2 Levitation control

The rotor needs to be levitated to verify the behavior of system using measured frequency responses. A conventional control system architecture is used to control the levitated position. The motor parameters from simulations are used to design the controller for initial levitation. Once the system is levitated, the frequency response can be obtained to verify the accuracy of the modelling and allow controller tuning. The control system architecture and related coordinate transformations for motor are shown in Fig 7.

The suspension winding currents are derived using the position signal error and the rotor angle to generate

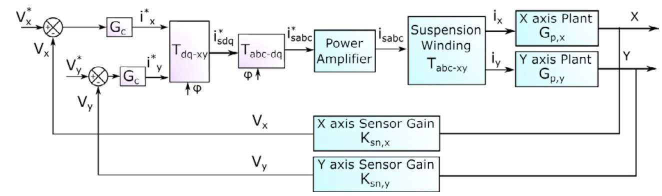

Fig. 7. Block diagram for closed-loop position control of levitated IPM motor showing the physical system (amplifier, motor and sensor) and control system. An equivalent voltage value is used as position reference.

the required force to keep the rotor in center. For 2 pole rotor the suspension winding is 4 pole and the proper commutation algorithm is developed as described in (1), (2) and (3). The forces have to be generated in 2 dimensions and hence 2 axis are chosen as X and Y which are in line with optical sensor. To generate the force in X/Y direction, the corresponding three phase currents can be obtained as shown in commutation algorithm (1), (2) and (3).

$$\begin{bmatrix} i_d \\ i_q \end{bmatrix} = \begin{bmatrix} \cos(\theta) & \sin(\theta) \\ -\sin(\theta) & \cos(\theta) \end{bmatrix} \begin{bmatrix} i_x \\ i_y \end{bmatrix} \quad (1)$$

$$i_{dq} = T_{dq-xy} \cdot i_{xy}$$

$$\begin{bmatrix} i_A \\ i_B \\ i_C \end{bmatrix} = \sqrt{\frac{2}{3}} \begin{bmatrix} 1 & 0 \\ -\frac{1}{2} & \frac{\sqrt{3}}{2} \\ -\frac{1}{2} & -\frac{\sqrt{3}}{2} \end{bmatrix} \begin{bmatrix} i_{s\alpha} \\ i_{s\beta} \end{bmatrix} \quad (2)$$

$$\begin{bmatrix} i_{s\alpha} \\ i_{s\beta} \end{bmatrix} = \begin{bmatrix} \cos(2\phi - \pi/6) & -\sin(2\phi - \pi/6) \\ \sin(2\phi - \pi/6) & \cos(2\phi - \pi/6) \end{bmatrix} \begin{bmatrix} i_{sd} \\ i_{sq} \end{bmatrix} \quad (3)$$

$$i_{ABC} = T_{ABC-\alpha\beta} \cdot T_{\alpha\beta-dq} \cdot i_{dq}$$

$$T_{ABC-dq} = T_{ABC-\alpha\beta} \cdot T_{\alpha\beta-dq}$$

5.3 Control System Design

A magnetically levitated system can be modeled as a spring mass system with negative spring stiffness as written below. These parameters for the motor are obtained from 3D FEM simulations. It helps in designing the controller. The data obtained from simulation and from experimental setup is shown in Table 1. The plant transfer function as specified in Fig. 7 can be written as

$$G_{p,x} = \frac{K_{fx}}{ms^2 - K_{sx}}, \; G_{p,y} = \frac{K_{fy}}{ms^2 - K_{sy}}$$

where, $G_{p,xy}$ are X and Y plant transfer function, K_{fxy} is the force constant(N/A_{rms}) in X and Y direction, m is the mass of the rotor, K_{sxy} is the negative stiffness(N/m) in the X and Y directions.

Table 1.

Parameter	**Value**
X Stiffness, $K_{sx}(N/m)$	22.5×10^3
Y Stiffness, $K_{sy}(N/m)$	23.3×10^3
X Force Constant, $K_{fx}(N/A\ in\ i_X)$	6.8
Y Force Constant, $K_{fy}(N/A\ in\ i_Y)$	9.3
X Sensor Gain, $K_{snx}(V/m)$	4.23×10^3
Y Sensor Gain, $K_{sny}(V/m)$	4.43×10^3
Rotor mass, $m(kg)$	0.15

The frequency response of the modeled plant with parameters obtained from FEM simulations is shown in Fig. 8.

The unstable frequency of the levitated rotor in orthogonal directions can be calculated as $\sqrt{(K_{sx/y}/m)}$ which in this case is 60.63 Hz and 61.7 Hz in X and Y. The suspension control system has to be designed faster than that which leads to a bandwidth specification of 200Hz. Looking at the plant frequency response, the controller architecture should include a phase lead compensator to attain required phase margin, gain to attain crossover frequency and a low pass filter to provide attenuation in the high frequency region. The structure is similar to what was used in (7). The controller used for both X and Y positions can be formulated as:

$$G_c = K_p \frac{\alpha\tau s + 1}{\frac{s^2}{\omega_0^2} + \frac{2\zeta s}{\omega_0} + 1}$$

where $K_p = 2.4418,\ \alpha = 6,\ \tau = 3.24249 \times 10^{-4},\ \omega_0 = 6156,\ \zeta = 0.7$.

The frequency response of the modeled loop return ratio is shown in Fig. 9. From this Figure, the position loop bandwidth can be seen as $114Hz$ with a phase margin of 45° approximately and Y position bandwidth of $160Hz$ with a 50° phase margin. These difference in the performance is mostly due to different stiffness and force constant in X and Y directions.

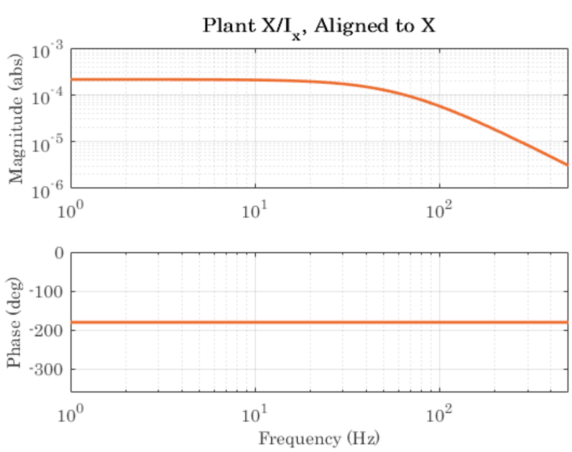

Fig. 8. Modelled frequency response of levitated system plant for X axis. The parameters I_x and X corresponds to the control system shown in Fig. 6.

5.4 Experimental Results

To verify the control design, the closed-loop levitated rotor is tested for step response in X direction while the rotor magnetic axis aligned to X axis. The step response corresponding to a 0.1 V sensor voltage input to X position is obtained and is shown in Fig. 11. A small coupling in X and Y position response can be seen from the results. Since the controller doesn't have an integrator, there is a steady state error in the position in response to a step command. But since the 0.1V sensor voltage step corresponds to 23.6 μm in X, the steady state position error doesn't affect the operation in any significant manner. The peak overshoots

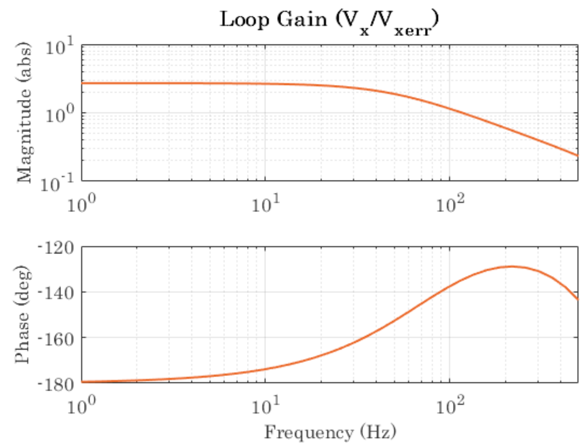

Fig. 9. Modelled frequency response of X axis levitation control system loop return ratio. The crossover frequency of 114 Hz and phase margin of 45° for X axis levitation control is measured from this plot.

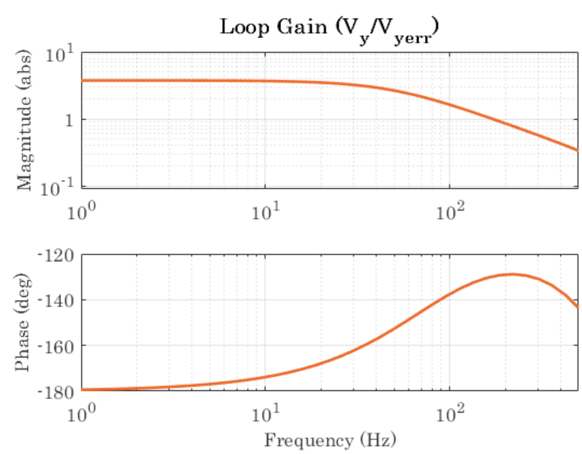

Fig. 10. Modelled frequency response of Y axis levitation control system loop return ratio. The crossover frequency of 160 Hz and phase margin of 50° for Y axis levitation control is measured from this plot.

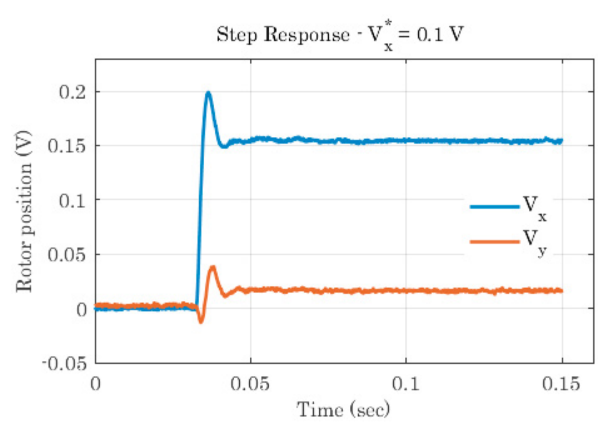

Fig. 11. Experimentally measured step response of X axis position control with 0.1V reference step voltage. A small coupling between X and Y position can be seen. Steady state position error can also be seen as there is no integration in the control.

in position can be understood using an approximate rule which defines that the damping ratio of a second order system can be approximated as $\zeta = \phi_m(°)/100$. This gives $\zeta_x = 0.45$ and hence the peak overshoot of 20% in X position which matches approximately the experimental results. A small increase in the Y axis position in steady state can be seen which is due to that fact that the rotor has very small cogging torque and it is difficult to hold it in one angular position during step response.

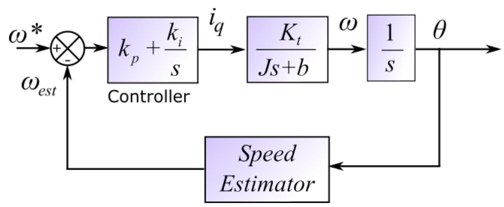

Fig. 12. Motor speed controller with speed feedback from estimator. PI controller parameters are $K_p = 0.005$ and $K_i = 0.01$. Only q axis current is used for speed control since the large airgap and the pump operation makes flux weakening unimportant.

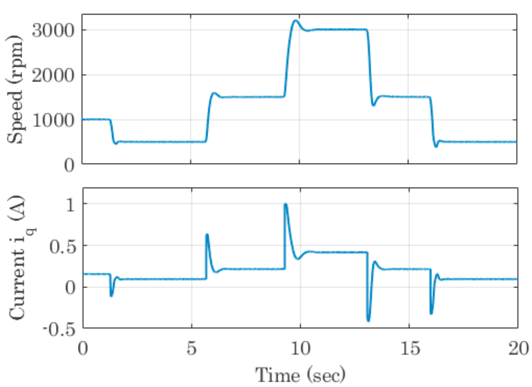

Fig. 13. Experimental closed-loop speed control performance with varying speed reference at no load. The current command is also shown.

5.5 Speed Control

For pump applications, the motor should be able to run at different speeds to regulate pressure and/or flow. Thus closed loop speed control is also implemented for this motor. Since there is no direct speed measurement, the motor speed is estimated using the angular position measurement obtained from Hall effect sensors.

This speed estimator is used for the closed loop speed control which is shown in Fig. 12. The speed control is similar to permanent magnet motors with only q-axis current control. A PI controller is used for the speed control and generating the current command. The closed loop speed control result with varying speed command is shown in Fig. 13.

6. CONCLUSION

A 2 pole bearingless interior permanent magnet motor is presented in this paper along with the rotor design using finite element simulation. The final motor force, torque capabilities and magnetic stiffness are estimated from simulations. The control system for levitation and speed control is designed using these parameters and verified with experimental results. The experimental step response for levitation control matches closely with the modelled frequency response. The speed control is also demonstrated experimentally with varying speed command.

ACKNOWLEDGEMENTS

The authors are thankful to Dr. Minkyun Noh for developing the earlier motor version and the base case motor used in this paper. We also thank Jeff Speakman for fabricating the rotor.

REFERENCES

[1] R. Schob and N. Barletta. Principle and Application of a Bearingless Slice Motor. In Proceedings of the 5th International Symposium on Magnetic Bearings, page 6, Kanazawa, Japan, August 1996.

[2] M. Noh, W. Gruber and D. L. Trumper, "Hysteresis Bearingless Slice Motors With Homopolar Flux-Biasing," in IEEE/ASME Transactions on Mechatronics, vol. 22, no. 5, pp. 2308-2318, Oct. 2017.

[3] M. Takemoto, M. Uyama, A. Chiba, H. Akagi, and T. Fukao. A deeply-buried permanent magnet bearingless motor with 2-pole motor windings and 4-pole suspension windings. In 38th IAS Annual Meeting on Conference Record of the Industry Applications Conference, volume 2, pages 1413-1420,October 2003.

[4] A. Chiba, T. Fukao, O. Ichikawa, M. Oshima, M. Takemoto, and D. G. Dorrell. Magnetic bearings and bearingless drives. Elsevier/Newnes, Amsterdam London, 2005.

[5] K. Raggl, T. Nussbaumer, J. W. Kolar, Comparison of Separated and Combined Winding Concepts for Bearingless Centrifugal Pumps, JPE Journal of Power Electronics, Vol. 9, No. 2, pp. 243-258, February 2009.

[6] R. Schöb, N. Barletta, J. Hahn, The Bearingless Centrifugal Pump - A Perfect Example of a Mechatronics System, IFAC Proceedings Volumes, Volume 33, Issue 26, 2000, Pages 443-448.

[7] B. S. Weinreb. A Novel Magnetically Levitated Interior Permanent Magnet Slice Motor. Doctoral Thesis, Massachusetts Institute of Technology, Cambridge, MA, USA, May 2020.

[8] B. S. Weinreb, M. Noh, D. Fyler and D. L. Trumper, "Design and implementation of a novel interior permanent magnet bearingless slice motor," in IEEE Transactions on Industry Applications.

[9] K. Kant, D. L. Trumper, " Rotor design for 2 Pole Bearingless Interior Permanent Magnet Slice motor," Accepted for publication in 2021 IEEE Energy Conversion Congress and Exposition (ECCE), Vancouver, Canada.

[10] M. Noh and D. L. Trumper, "Homopolar Bearingless Slice Motor With Flux-Biasing Halbach Arrays," in IEEE Transactions on Industrial Electronics, vol. 67, no. 9, pp. 7757-7766, Sept. 2020.